The beauty of being complex

Khasevani, SG; Nikjoo, D; Ojwang, DO; Nodari, L; Sarmad, S; Mikkola, JP; Rigoni, F; Concina, I

Published in:
Journal of Catalysis

Published: 01/06/2022

Document Version
Final published version

Document License
CC BY

Journal of Catalysis 410 (2022) 307–319

Contents lists available at ScienceDirect

Journal of Catalysis

journal homepage: www.elsevier.com/locate/jcat

The beauty of being complex: Prussian blue analogues as selective catalysts and photocatalysts in the degradation of ciprofloxacin

Sepideh G. Khasevani [a,1], Dariush Nikjoo [a,1], Dickson O. Ojwang [b], Luca Nodari [c,d], Shokat Sarmad [e], Jyri-Pekka Mikkola [e,f], Federica Rigoni [g], Isabella Concina [a,*]

[a] Luleå University of Technology, Department of Engineering Sciences and Mathematics, 98187 Luleå, Sweden
[b] Department of Chemistry – Ångström Laboratory, Uppsala University, Box 538, SE-751 21 Uppsala, Sweden
[c] Dipartimento di Scienze Chimiche, Università degli Studi di Padova, 35131 Padova, Italy
[d] Istituto di Chimica della Materia Condensata e di Tecnologie per l'Energia, ICMATE-CNR, 35127 Padova, Italy
[e] Technical Chemistry, Department of Chemistry, Chemical-Biological Centre, Umeå University, SE-90871 Umeå, Sweden
[f] Industrial Chemistry & Reaction Engineering, John Gadolin Process Chemistry Centre, Åbo Akademi University, Biskopsgatan 8, FI-20500 Åbo-Turku, Finland
[g] Department of Molecular Sciences and Nanosystems, Ca' Foscari University of Venice, 30170 Venezia-Mestre, Italy

ARTICLE INFO

Article history:
Received 11 January 2022
Revised 23 March 2022
Accepted 27 April 2022
Available online 30 April 2022

Keywords:
Prussian blue analogues
Ciprofloxacin degradation
Photocatalysis
Auto-catalytic reactions
Mössbauer spectroscopy

ABSTRACT

We investigate the performance of four Prussian blue analogues (PBAs) as catalysts for the selective degradation of ciprofloxacin in water, under both dark and illumination conditions. We show that no light is actually needed to induce a selective degradation of the molecular target, while light irradiation spurs the process, without, however, resulting in the commonly reported photolysis-supported breaking down. We present a systematic characterization of the PBAs aiming at interpreting the catalytic outcomes in the light of a classic coordination chemistry analysis, empowered by the most recent findings in literature. We show that varying the transition metal binding the N atom of the cyanide bridge is key to promote photoinduced charge generation and transfer, which effectively disrupts the molecular target. The analysis of the materials before and after the irradiation with solar simulated light results in a change of the lattice parameters, indicating the possibility of a light-induced spin cross-over.

1. Introduction

Prussian blue analogues (PBAs) are attracting an increasing interest within the scientific community engaged in the search for both effective catalysts and photocatalysts in water oxidation [1] as well as materials for batteries and chemical capacitors [2,3]. The characteristics making these systems particularly interesting are related to their atomic structures as well as their ionic and electronic properties. In coordination chemistry, Prussian blue (PB) (either in the so-called soluble form $KFe^{III}[Fe^{II}(CN)_6]\cdot xH_2O$ or the alternative insoluble $Fe^{III}_4[Fe^{II}(CN)_6]_3\cdot xH_2O$) represents the classic example of a mixed valence coordination complex, its color originating from an intervalent charge transfer of an electron from Fe^{II} to Fe^{III}. This oxidation states cross-talk, together with the possibility to easily synthesize analogues in which one or both iron atoms can be substituted by other transition metals, has a remarkable potential in catalysis. However, most literature available on the catalytic performance of PBAs focused on their application as agents to promote water oxidation, while other processes are seldomly considered (some examples are provided in references [4–7]). In this respect, PBAs have recently been proved effective photo-Fenton catalysts for the degradation of Rhodamine B in water [6], bisphenol-A, methylene blue and humic acid [8]: upon irradiation they are capable of generating reactive oxygen species which are then effective in oxidizing the molecular pollutants. Little is however still known about their action as catalysts in dark conditions.

It should be pointed out that the investigation of PBAs is no trivial subject, although the forefather of this class of materials was studied since early 18th century [9,10], many aspects of metal complexes, including their structure, photoinduced charge transfer and other features relevant to functional applications, were investigated only recently, thanks to the development of specific analytical techniques, and much still remains to clarify about these fascinating inorganic compounds.

The PB structure is characterized by metal cations connected through cyanide ligands acting as bridges between them, presenting the general formula $A_nM_y[M'(CN)_6]\cdot xH_2O$, where A is an alkali

* Corresponding author at: Luleå University of Technology, Department of Engineering Sciences and Mathematics, Division of Materials Science, 98187 Luleå, Sweden.
[1] These authors equally contributed to the present work.

https://doi.org/10.1016/j.jcat.2022.04.029
0021-9517/

metal, and both M and M' are transition metals. The relative amounts of A, M and M', as well as the number of water molecules present in the structure, strongly depend on the synthetic history of the compounds and also on the storage conditions, which renders it mandatory to perform a careful characterization, case by case, of the material under investigation.

The basic chemical unit of PBAs (sketched in Fig. 1) consists of an iron atom coordinated to six cyanide ligands through the carbon atom, which bridges the other transition metal by the nitrogen atom.

The coordination sphere of M features instead the general formula $MII(NC)_x(OH_2)_{6-x}$. The water molecules acting as ligands can dissociate and leave space for M to bind other species present in the surrounding environment, featuring a stronger ligand capability (which is possible to think of according to the spectrochemical series). The possibility of tuning the nature of M, inserting in the basic PB structure a transition metal with reversible redox capability, is the trigger to exploit these materials as catalysts, completed by the capability of the C ≡ N bridges to shuttle charges between the transition metals, M and M′, and to the presence of coordinated water molecules, completing the coordination sphere of M. Indeed, M is the catalytically active site to which the catalytic molecular targets binds (via either associative or dissociative mechanism), and replaces the water molecule(s). From a classical perspective considering the use of coordination complexes as catalysts, having a transition metal located at that site, capable of featuring different stable oxidation states, is the key to spur the desired chemical transformations of the molecular targets.

In the present investigation, we prepared four PBAs via co-precipitation, namely iron hexacyanoferrate (abbreviated as FeHCF), manganese, cobalt, and copper ferricyanides (abbreviated as MnHCF, CoHCF and CuHCF, respectively) and investigated their performance as catalysts towards the degradation of ciprofloxacin (CIP) in water, under both dark and simulated solar light conditions. CIP is chosen as a molecular model for antibiotics belonging to the fluoroquinolone class, whose presence in surface and ground waters is a cause of concern in many countries. Their degradation is a process of great interest and has recently attracted considerable attention, especially focusing on photolysis supported by inorganic oxidants and photocatalysts [11–14]. Several investigations have indeed appeared dealing with attempts to remove them from water by using different classes of (photo)catalysts, including free radicals [15] and nanosized semiconducting metal oxides [16–19]. However, very little is reported about the use of coordination complexes to pursue the removal of these organics [20], although PB and PBAs are acknowledged as activators of C—H bonds in amines [21].

While all the PBAs show a selective action as catalysts, resulting in the presence of only one degradation product in the reaction mixture, we found different behaviors associated to different PBAs, which were then deeply characterized, aimed at elucidating the reasons behind the observed differences.

2. Experimental

2.1. Synthesis of Prussian blue (PB) and Prussian blue analogues (PBAs)

Prussian blue ($Fe^{III}[Fe^{II}(CN)_6]_{3/4}\cdot xH_2O$) was synthesized through the simultaneous dropwise addition of 100 mL of $Fe(NO_3)_3\cdot 9H_2O$ (0.04 M) and 100 mL of $K_4Fe(CN)_6$ (0.02 M) to 25 mL of distilled water under constant stirring at room temperature. A dark blue precipitate formed immediately. The resulting precipitates were centrifuged and dried in a vacuum oven at 60 °C for 12 h. The stoichiometric proportions of the resulting phase can be expressed as:

$$Fe^{3+}{}_{(aq)} + 3/4[Fe^{II}(CN)_6]^{4-}{}_{(aq)}\ Fe^{III}[Fe^{II}(CN)_6]_{3/4}\cdot xH_2O_{(s)}$$

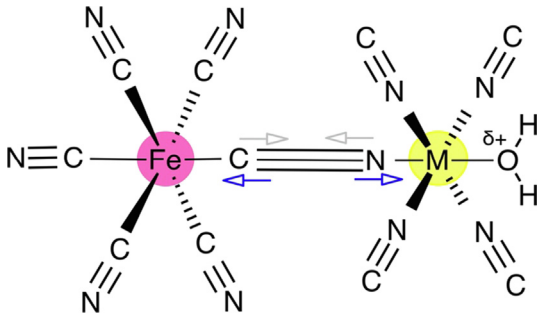

Fig. 1. Features of the basic chemical units in a PBA. The blue and grey arrows indicate the σ donation and π back-donation from the C ≡ N ligand, respectively. The distance between the iron atom and M is about 5 Å. The catalytic active site is M. (For interpretation of the references to color in this figure legend, the reader is referred to the web version of this article.)

For the preparation of PBAs, $X^{II}[Fe^{III}(CN)_6]_{2/3}\cdot xH_2O$ (X = Co, Cu, and Mn); equal volumes, 50 mL of $X(NO_3)_2$ (0.08 M) and $K_3Fe(CN)_6$ (0.04 M) solutions were simultaneously mixed in 25 mL of distilled water under constant stirring at room temperature. The resulting precipitates were centrifuged and dried in a vacuum oven at 60 °C for 12 h. The stoichiometric proportions of the resulting compounds can be expressed as:

$$X^{2+}{}_{(aq)} + 2/3[Fe^{III}(CN)_6]^{3-}{}_{(aq)}\ X^{II}[Fe^{III}(CN)_6]_{2/3}\cdot xH_2O_{(s)}$$

All the chemicals were purchased from Sigma-Aldrich and used without any further purification.

2.2. Thermal analyses

Thermogravimetric analysis (TGA) and differential scanning calorimetry (DSC) were performed using a STA 449C Jupiter (NETZSCH, Germany) instrument. Each sample (5–10 mg) was heated from 25 to 500 °C at a rate of 10 °C min^{-1} under flowing argon gas.

2.3. X-ray diffraction (XRD) analysis

Powder XRD patterns of the samples were recorded on a PANalytical Empyrean instrument equipped with a PIXcel3D detector and operated at 40 kV and 45 mA using Cu-Kα radiation. The obtained results were analyzed using High Score Plus software (vers.3.0.1). To calculate the cell parameter *a*, first the interplanar spacing *d* was calculated, from Bragg's law ($n\lambda = 2d\sin\theta$), considering $n = 1$ and $\lambda = 1.5406$ Å. Then, from Miller indices *h, k, l*, one obtains: $a = d\sqrt{h^2 + k^2 + l^2}$. The error on the angle is given by the experimental spectral resolution (0.026°) and propagated to obtain the error in the cell parameter *a*. Results reported in Table S2 in the Supporting Information are related to 200 peak. Data were compared with ICSD reference XRD database.

2.4. Fourier transform infrared (FTIR) spectroscopy

An attenuated total reflectance Fourier transform–infrared (ATR-FTIR) spectroscopic technique was performed using a Bruker VERTEX 80v FTIR spectrometer (Germany). Each sample was analyzed in the range 4000–400 cm^{-1} by averaging 128 scans at a spectral resolution of 4 cm^{-1}.

2.5. Electron microscopy

Energy-dispersive X-ray spectroscopy (EDX) was carried out in a scanning electron microscope (JSM-IT300). AZtech Oxford

software was used for the extraction of EDX results from the raw data. The appropriate amount of the samples was mounted on a metal plate by a Leit-C conductive carbon (Plano GmbH, Wetzlar, Germany) prior to insertion into the microscope.

2.6. High performance liquid chromatography

10 μL of the reaction mixture after the catalytic tests were injected into a Hypersil gold C18 column (2.1 × 50 mm with 1.9 μm particle size) using an auto-injector (Thermo Finnigan). As the mobile phase, a mixture of water (solvent A) and acetonitrile (solvent B), both containing 0.1% (v/v) of formic acid, was used. The applied gradient for the mobile phase is reported in Table 1:

A LCQ FLEET ion-trap mass spectrometer (Thermo Finnigan) was used together with an electrospray ion source in positive ion mode. Samples were tested as received.

2.7. Mössbauer spectroscopy

Room Temperature (RT) ^{57}Fe Mössbauer spectroscopy was performed on a conventional constant acceleration spectrometer mounting a Rh matrix ^{57}Co source, nominal strength 1850 MBq. The absorber was prepared by mixing ≈70 mg of sample with petroleum jelly. The spectra were fitted to Lorentzian line shapes with the minimum number of components by using Recoil software [22]. Hyperfine parameters were obtained by means of standard least-squares minimization techniques; isomer shift (δ), quadrupole splitting (Δ), half linewidth at half maximum (Γ_+), were expressed in mms^{-1}, the relative area (A) in %. δ is quoted relative to RT α-Fe foil.

2.8. Photocatalytic degradation tests

Catalytic degradation of 10 ppm aqueous solution of ciprofloxacin (ACROS Co.) was carried out at room temperature under both dark and irradiation conditions. 10 mg of catalyst were added to the CIP solution in each experiment.

Light irradiation was performed using a LOT-QD solar simulator (AM1.5G spectrum at 1 sun intensity, calibrated with a silicon reference cell). Aliquots of the reaction mixtures were extracted at specific times and analyzed through spectrophotometry (Agilent Cary 5000 spectrophotometer), to determine the CIP concentration by monitoring the evolution of the peak centered at 271 nm.

3. Results and discussion

3.1. Catalytic degradation of ciprofloxacin

Fig. 2 reports the reaction course, plotted as C/C_0, of CIP degradation under dark (Fig. 2a), followed by exposure to solar simulated light (Fig. 2b) and under light exposure without any dark period (Fig. 2c), where C is the molar concentration detected at a given reaction time and C_0 is the initial CIP concentration.

The usual approach in a heterogeneous photocatalytic experiment is to stir the molecular target in the solution with the catalyst for a certain amount of time (usually 30 min) prior to light irradiation, to ensure the equilibrium between adsorption/desorption of the molecule on the catalyst surface. However, we decided to investigate a longer dark period, since the PBAs have the potential to be active as catalysts without the need of any light, due to their coordination chemistry nature. Analysis of the reaction course under dark (Fig. 2a) shows, indeed, that no equilibrium is reached, even after 150 min. All the analogues degrade CIP in an amount as high as about 30% in 150 min (except for CoHCF, for which less than 10% CIP decrease is detected). The degradation reaction is then further monitored for 180 min under simulated solar light (Fig. 2b). During this time FeHCF and CuHCF degrade an additional 40% of the target molecule, whereas MnHCF and CoHCF feature a significantly better efficiency and remove about 80% of the residual CIP. Finally, we monitored the degradation of CIP by switching ON the simulated solar light immediately after the catalyst was added to the CIP solution in water (Fig. 2c), observing a different behavior compared to what was recorded in both the previous experiments. CoHCF shows an excellent performance, degrading around 70% of the initial CIP concentration in 30 min, while all the other PBAs, although characterized by different kinetics, can remove only 50% of the target molecule after 3 h.

The observed behavior under dark implies two relevant consequences: i) all the materials are active catalysts under dark conditions (no light is actually needed to initiate the catalytic process) and ii) when the light is switched ON after the dark period, there already is some reaction product in the reaction mixture. It is also notable that, although the materials are active under dark, the illumination undoubtedly spurs the process.

We can thus identify different behaviors depending on the reaction conditions (light OFF, light ON), as well as differences among the catalysts. However, all the systems reach a steady state after about 2 h under illumination. These observations are summarized in Table 2, where we also report the values for the turnover number (TON) for each catalyst. The TON values indicate we are observing a catalytic process under all the investigated experimental conditions.

Table 1
Gradient of the mobile phase used in LC-MS analysis.

Time (min)	A%	B%	Flow rate (μL/min)
0	95	5	250
0.3	95	5	250
1.7	70	30	350
8	0	100	350
10	0	100	350
11	95	5	250
12	95	5	250

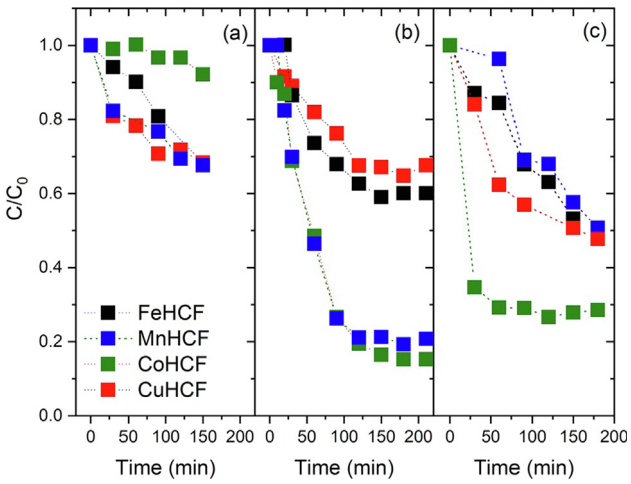

Fig. 2. Reaction course plotted as CIP relative concentration C/C_0 for the investigated materials under (a) dark and (b) solar simulated light. (c) Reaction course under solar simulated light without any dark period prior to light ON. Black markers: FeHCF; blue markers: MnHCF; green markers: CoHCF; red markers: CuHCF. Markers are experimental points; lines are guide for the eye. (For interpretation of the references to color in this figure legend, the reader is referred to the web version of this article.)

Table 2
Catalytic performance towards CIP degradation of the investigated materials under dark, upon simulated solar light (after dark period) and under simulated solar light with no previous dark period. § The turnover number (TON) is calculated as $\frac{molCIPdegraded}{molcatalyst}$.

Catalyst	% Degradation (150 min light OFF)	% Degradation (120 min light ON)	% Degradation (120 min only light)	TON§ dark	TON§ light	TON§ only light
FeHCF	31.7	31.2	36.9	1023	964	939
CoHCF	7.90	80.5	73.3	193	1696	1360
CuHCF	31.6	32.4	39.4	634	444	687
MnHCF	32.3	78.9	32.0	788	1322	605

The analysis of the semilog plots of the reaction course, displayed in Figure S1 in the Supporting Information, shows no obvious trend. In particular, the behavior of FeHCF under dark seems to evidence a (pseudo)zero order reaction, while all the PBAs show a pseudo-first order reaction under dark and a sigmoid trend under irradiation. We then fitted all the curves with the most appropriate equations (see Table S1 in the Supporting Information), namely a line, an exponential, and a sigmoid (logistic function), reported as Equations 1–3 in the Supporting Information.

A linear trend, suggesting a process following a zero (or pseudo-zero) reaction, is quite unusual: it would mean the reaction rate does not depend on the initial concentration of the molecular target. We then decided to verify this trend by carrying out additional tests, where the initial CIP concentration was varied (the experimental outcomes are shown in Figure S2 in the Supporting Information). The linear trend is confirmed for CIP concentrations ranging from 10 to 5 ppm. Below this latter concentration (down to 3 ppm), the reaction course shows a different behavior, which however is not possible to fit by a single equation, but consists of two different contributions (linear from 0 min to 60 min). Moreover, an extension in reaction time confirms the linear trend over 5 h (Figure S3 in the Supporting Information).

The sigmoid trend recorded for all the catalysts upon light irradiation (following a dark period) indicates that we are observing an auto-catalytic reaction, like the following:

$$A + Z \rightarrow Z + \ldots$$

where A is the molecular target (CIP) and Z is one of the reaction products.

In auto-catalytic processes, a reaction product appears in the rate equation for the forward reaction [23], whose order cannot be determined just by looking at the overall process.

This reaction features a second-order rate equation, leading to the following integrated equation:

$$ln\frac{c_Z}{c_A} = (c_A^0 + c_Z^0)kt + ln\frac{c_Z^0}{c_A^0} \quad (1)$$

The solution of Eq. (1) is indeed an expression where the concentration is a sigmoid (typically a logistic) function of the time. This trend, confirmed in all our experiments, is coherent with the presence of some reaction product in the mixture after the dark period, which furthermore confirms that all the PBAs are active as catalysts also under dark. The induction time is similar for FeHCF, MnHCF, and CoHCF, while it is shorter for CuHCF.

In order to evaluate the actual behaviors of the PBAs as catalysts under light irradiation, we then carried out further experiments, for which the solar simulator was switched ON immediately after the insertion of PBAs in the CIP solution. For these experiments the initial CIP concentration was set as the initial concentration of the former light test after the dark period (to avoid possible ambiguity due to pseudo-first order reactions). The results, reported in Figure S4 in the Supporting Information, are quite surprising. When the CIP degradation is catalyzed by FeHCF (Figure S4 a and b), a linear trend is observed once again, with half the initial CIP amount being consumed after 150 min, with an apparent rate constant of 0.00413 min^{-1}. MnHCF (Figure S4 c and d) features a different behavior, that requires two fitting equations accounting for the whole time during which the CIP degradation is monitored. This is due to a partial dissolution of MnHCF in the reaction mixture (as inferred by the absorption spectra reported in Figure S5 of the Supporting Information): the reaction is thus catalyzed in both homogeneous and heterogeneous fashion. We believe that at the beginning a homogeneous catalysis occurs (MnHCF dissolution takes place immediately as the light is switched ON), which is then taken over by the heterogeneous process. This hypothesis is also supported by the values of the apparent rate constants retrieved from the fitting: a fast process (0.0640 min^{-1}) is followed by a slower one (0.00145 min^{-1}), which is coherent with the first one being supported in a homogeneous (or mixed) way and the second being mostly heterogeneous.

The catalytic action of CoHCF (in Figure S4 e and f), instead, is clearly following a single exponential trend and is moreover extremely fast (75% of the initial CIP amount is degraded in 30 min, with an apparent rate constant as high as 0.05931 min^{-1}, an order of magnitude higher than that recorded for FeHCF) and much faster than the same reaction carried out after a dark period. The reaction neither obeys a (pseudo)-second order law, nor a third-order: its kinetics is more complex and could not be disclosed.

The reaction catalyzed by CuHCF also features an exponential trend (Figure S4 g and h), with an apparent rate constant as high as 0.0123 min^{-1}.

In summary, it is possible to observe the following: (i) all the materials are photoactivated; (ii) FeHCF, MnHCF, and CuHCF can degrade about 50% of the initial CIP amount in 3 h; (iii) the reaction catalyzed by FeHCF follows a pseudo-zero order rate law, while all the PBAs feature a more complex kinetics (beyond third-order); (iv) CoHCF shows a particularly high activity towards CIP degradation, with 70% of the initial amount being degraded during the first 30 min. A summary of the calculated apparent rate constants is shown in Table 3).

Aiming at understanding and semi-quantifying the observed different trends, we then analyzed each and every reaction, looking for rate constants and reaction orders. We moreover analyzed the reaction mixtures by means of HPLC-MS to identify the products generated by each material. In spite of the differences observed for the kinetics, the analysis of the reaction mixtures carried out by HPLC coupled with mass spectrometry (reported in Figures S6 and S7 in the Supporting Material) only shows one reaction product in all cases, whose definitive identification is, however, made hard by the unavailability of standards (as previously remarked in literature). When the reaction is carried out under dark with FeHCF, a compound featuring a parent ion with m/z ratio of 332 is observed. A chemical with the same m/z ratio and a similar fragmentation pathways was identified by Salma and collaborators in 2016 [11], who carried out the direct CIP photolysis and retrieved its chemical formula as $C_{16}H_{17}N_3O_5$. The same product is found when the reaction is supported by light irradiation and the catalysts used are CoHCF and MnHCF. When instead the reaction is cat-

Table 3
Apparent rate constants for CIP degradation under simulated solar light. The fitting equations used for each material are reported in the Supporting Information (Equations 1–3).

Sample	Apparent rate constant ($min^{-1} \times 10^2$)	Degradation after 180 min (%)
FeHCF	0.413 (R^2 = 0.974)	46.8
MnHCF	6.40 (R^2 = 0.997)1.45 (R^2 = 0.964)	49.2
CoHCF	5.93 (R^2 = 0.997)	71.4
CuHCF	1.23 (R^2 = 0.981)	52.3

alyzed by FeHCF and CuHCF upon light irradiation, a different reaction product is observed (Figure S6 c and d), which we identified as the dehydroxylated CIP derivative. These findings show that PBAs are quite selective catalysts, and that direct CIP photolysis is not the main path involved in its degradation, contrary to what observed in all the previous investigations reported in literature.

We attempt herein an interpretation of the catalytic results by applying the classic analysis of the catalytic action of coordination complexes. Regardless of the catalytic mechanism, the first step of the process is to find space for the molecular target to bind with the metal complex, i.e., the molecule should possess a functional group able to act as a ligand for the complex. While CIP brings several functional groups potentially suitable for this, the carboxylic function (with or without the hydrogen atom) can fulfill this role the best, especially for the position (not hindered) it occupies in the molecular structure, with the additional benefit of the potential of chelating, thus adding stability to the formed adduct. As mentioned, the PBAs can have structural vacancies (that we will analyze in the following sections) that leave space for water molecules to coordinate to M (see Fig. 1). This specific site is particularly suited for catalysis. Indeed, water is a weak ligand, which can be easily substituted by a more powerful actor.

Aiming at understanding both how the PBAs exert their catalytic action, and why relevant differences are observed, a detailed materials characterization, before and after the interaction with CIP is carried out.

3.2. Absorption spectra

The analysis of the absorption spectrum is relevant for understanding what happens in terms of charge transfer when the PBAs are used as photocatalysts. As known, the electronic spectra of PBA complexes arise from two different processes; internal transitions of electrons in the incomplete d shell of the metal ion, and the so-called charge transfers, involving the transfer of an electron from the metal to the ligand and *vice-versa*. These latter are usually broader and found at higher energy than the internal transitions and often only the edge of the band is observed. However, PBAs represent a very peculiar case in the big family of metal complexes, due to the mentioned ability of the C≡N ligand in shuttling electrons.

The absorption spectra in water of all the materials show the bands expected for the $[Fe(CN)_6]$ unit (the spectrum of FeHCF is reported in Fig. 3 a as the representative of the batch), with very small differences in energies ascribable to the substitution of the iron bound to the N atom of the cyanide ligand with another transition metal (the spectra also reported as a function of wavelength in Figure S8 in the Supporting Information, to help the Reader in comparing the adsorption of PBAs with that of CIP). In particular, it is possible to identify the following spectral features: an asymmetric band centered around 24 000 cm^{-1}, ascribed to a ligand-to-metal charge-transfer transition; a more intense signal located at 33 000 cm^{-1}, surrounded by two shoulders (31 145 and 34 940 cm^{-1}), which is the octahedral splitting energy Δ_O between the t_2g and the e_g d-orbitals of the iron ion due to the ligand-induced crystal field; [24] an intense band at 38 280 cm^{-1}, which is the lowest crystal field transition energy $t_6 \rightarrow t_5e$ of the $[Fe(CN)_6]^{4-}$ complex [25,26]. On the other hand, the analysis of the reflectance spectrum of the samples in their solid form (displayed in Fig. 3 b) shows the presence of less characteristic bands, centered around 17 600, 25 380, 35 930 and 41 190 cm^{-1}, respectively.

3.3. Structure, lattice parameters and crystallite sizes

Powder XRD patterns of the materials investigated in the present study are shown in Figure S9 in the Supporting Information. All peaks of PBAs are indexed with a typical face-centered cubic structure with the space group, $Fm\bar{3}m$ [27].

After the catalytic tests, all the materials feature a discrete shift towards higher angles in their XRD patterns (reported as dotted lines for 200 and 220 peaks in Fig. 4). This indicates a systematic decrease in the unit cell size. The shift, although still visible, is very small for MnHCF.

The unit cell size was calculated for all the samples under investigation before and after the reaction (upon simulated solar light irradiation) and the results are shown in Table S2 in the Supporting Information (the histogram of the unit cell size before and after light exposure is reported in Figure S10 in the Supporting Information).

3.4. Chemical composition

The identification of the stoichiometry of PBAs is no trivial matter, depending on several parameters, including the preparation methods employed to synthesize them and their storage conditions. In order to determine the actual chemical nature of the PBAs under investigation, we took advantage of several analytical techniques, aiming at identifying and/or quantifying, i) the ratio between Fe/M content, ii) the water content (coordinated and zeolitic), and iii) the ratio between Fe^{II}/Fe^{III}.

EDX analysis is applied to quantify the metals and the nitrogen contents present in the PBA samples, whose values are given in Table 4. Compared to the amount of $M(NO_3)_2$ used in the syntheses (twice the concentration of $K_3[Fe(NO_3)_6]$), EDX results indicate that the ratio of both Mn and Co to Fe is 1.5, while it is slightly lower for Cu (1.39). The ratio of Fe to N content (equal to three for a stoichiometric compound) provides information about the presence of $[Fe(CN)_6]$ vacancies which is observed for all the materials studied.

The presence of water molecules, which play an important role in both determining the stoichiometry of these complexes and their optoelectronic features, was investigated by thermal analyses (TGA and DSC, reported in Fig. 5). The amount of water in PBAs can significantly vary, depending for instance on the synthesis, the presence of alkali metals, the storage, and thus the total water content is often not clearly quantified [28].

However, in all PBAs, water molecules are classified as of three different kinds: (i) the so-called zeolitic water (found in the cavities formed by the M′-CN-M framework), whose ideal number was reported as eight molecules per unit cell, (ii) coordinated water (which acts as a ligand to the M transition metal, by replacing the vacant $[Fe(CN)_6]$ octahedra), whose ideal number is as well eight molecules per unit cell and which is deeply involved in determining the catalytic activity of these materials (see Fig. 1), and (iii) hydrogen-bound water.

Thermal analyses allow for differentiating between the water molecules occupying zeolitic site of the crystalline lattice and those coordinated (which are released from the material at different temperature ranges), although the release of coordinated water

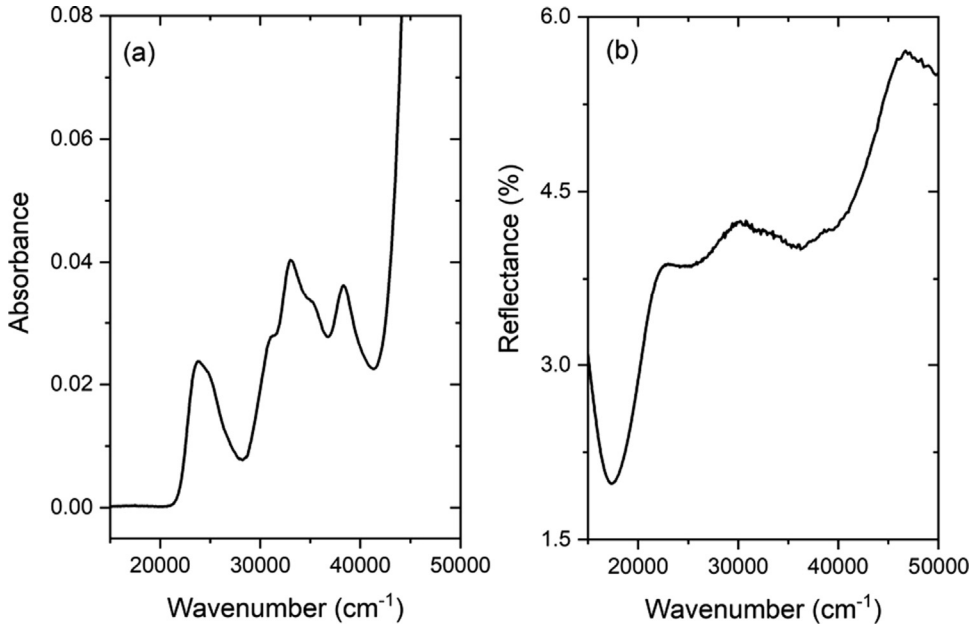

Fig. 3. Electronic absorption spectrum of FeHCF in (a) water and (b) solid state.

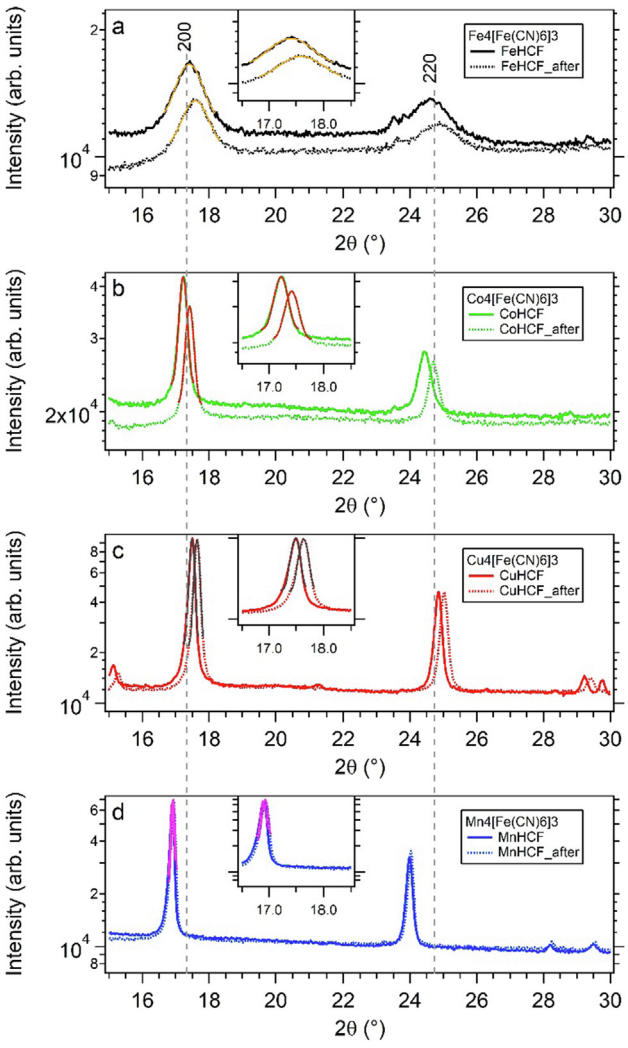

Fig. 4. Evolution of the XRD peaks at 200 and 220 before (solid lines) and after (dotted lines) the catalytic reactions of PB and its analogues.

molecules overlaps with the subsequent degradation at temperatures higher than 180 °C. Depending on M, water is released at different temperatures, as shown by thermal analyses reported in Fig. 5 and the region between 150 and 180 °C is of particular interest.

TGA analysis (Fig. 5 a) shows a weight loss, consisting of two contributions identified by DSC (Fig. 5 b), as high as about 20% from 30 to 150 °C for FeHCF and CuHCF (associated to an endothermic process, as evidenced by DSC analysis, shown in Fig. 5 b), which continues up to about 180 °C for CoHCF and MnHCF (for which, however, it is in continuity with the subsequent loss, associated to an exothermic process, as revealed by the DSC curves).

The total water content is found to vary along the PBA series, as shown in Table 5, which also reports the average number of coordinated water molecules for each material.

DSC analysis indicates that there are two endothermic processes associated with this mass loss, which can be ascribed to adsorbed water molecules and to coordinated water molecules, at increasing temperatures, respectively. At higher temperatures, other processes are observed in the DSC plot, whose interpretation was attempted in literature [29,30], with different degree of success. It is possible to ascribe the loss of $(CN)_2$ and CO_2 to the exothermic processes occurring at 204 °C and 309 °C, respectively, which correspond to an overall weight loss as high as 37.60%. However, it should be observed that an attempt of retrieving stoichiometric information out of these signals is quite difficult, since the nitrogen atoms originally belonging to the cyanide groups undergo oxidation to nitrogen oxides (NO and NO_2) at temperatures higher than 400 °C (not reported in Fig. 5 for clarity purposes) [31]. Based on these results, coupled with the EDX and XRD data, we could identify the following nominal formulas for the complexes: $K_{0.5}Fe_4[Fe(CN)_6]_3{\cdot}5.3H_2O$, $K_{0.2}Mn_3[Fe(CN)_6]_2{\cdot}7.3H_2O$, $K_{0.8}Co_3[Fe(CN)_6]_2{\cdot}5.5H_2O$, $K_{0.2}Cu_3[Fe(CN)_6]_2{\cdot}4.9H_2O$.

3.5. Infrared spectroscopy

Vibrational spectroscopy is acknowledged among the most powerful analytical techniques applicable to study the PBAs, providing much information about different sites of these complexes. Water molecules acting as ligands (substituting a missing C≡N

Table 4
EDX elemental analysis of the prepared materials.

Sample	K (Wt%)	Fe (Wt%)	M (Wt%)	N (Wt%)	M/Fe	Fe/N
FeHCF	10.00	40.12	–	14.70	–	2.73
MnHCF	2.36	25.60	39.58	10.34	1.54	2.48
CoHCF	7.93	18.73	29.57	12.67	1.58	1.48
CuHCF	3.21	26.82	41.30	12.12	1.39	2.21

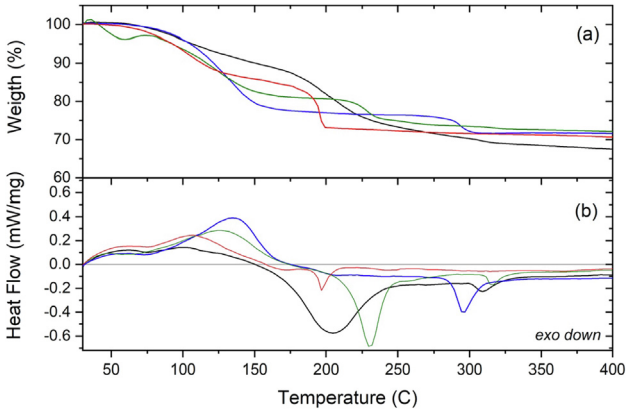

Fig. 5. TGA (a) and DSC (b) analysis of PBAs. Black line: FeHCF green line: CoHCF, red line: CuHCF, blue line: MnHCF. In DSC analysis, exothermal processes are directed downwards. (For interpretation of the references to color in this figure legend, the reader is referred to the web version of this article.)

coordinating M) or hydrogen-bonded exhibit different vibrational modes, thus their presence can be detected by infrared spectroscopy. The C ≡ N stretching vibration $\nu_{(C\equiv N)}$ is intense and very characteristic, its position moreover being very sensitive to the chemical environment. Furthermore, it becomes a doublet when both Fe^{II} and Fe^{III} are present, whose relative amount can be estimated by the analysis of this vibrational mode. FTIR analysis coupled with Mössbauer spectroscopy, provides the picture of status of iron within the samples. Even more interesting, the possibility to use FTIR to identify also the presence (and the oxidation state) of the second transition metal in the case of CoHCF complexes has been reported [32–34]. In the infrared region the vibrations Fe-C can be observed, which are also sensitive to the iron oxidation state, thus adding relevant information about both the strength of this bond among the PBAs and the possible changes induced by the interaction with CIP molecules. Even further, infrared spectroscopy has been proven as a powerful tool for monitoring the electronic transitions occurring in these complexes, especially due to light exposure. The $\nu_{(C\equiv N)}$ vibration is located in the 2200–2100 cm^{-1} spectral range. Its sensitivity to the surrounding environment is so extreme that it also includes the oxidation states and the spin states of the transition metal atoms bridged by this ligand [35]. While this vibrational mode is very rich in information (including the presence of minority species), the superimposition of several, usually small, contribution to the narrow $\nu_{(C\equiv N)}$spectral range may hinder this information. However, this issue may be partly overcome by analyzing the M-L vibrational bands. Our instrument cannot access the far infrared region where the M-N vibrations occur, but we could analyze the M-C spectral characteristics.

We then performed a careful analysis of the infrared spectra of the PBAs (the full mid-IR spectra are displayed in Figure S11 in the Supporting Information), reported in Table 6, and analyzed the detail of the C ≡ N stretching region (Fig. 6).

Observation of the C ≡ N stretching region and of the Fe-C vibrational modes before and after the catalytic tests (values are reported in Table 6) show no change in their positions (within the adopted instrumental resolution), indicating that the native chemical nature of the PBAs is untouched. However, the relative band intensities of the Fe(II) or Fe(III) - (C ≡ N) stretching appears modified after the catalytic reaction. Indeed the analysis of $\nu_{(C\equiv N)}$ allows to quantify the ratio between Fe(II) and Fe(III) in the complexes, before and after CIP degradation, as reported in Table 7 (the full FTIR spectra of PBAs after the catalytic tests are reported in Figure S12 in the Supporting Information). It is remarkable to note that the observed presence of Fe(II) in all the PBAs before the reaction with CIP indicates a natural charge exchange between the two transition metal species, resulting in mixed valence complexes. This finding is moreover supported by the analysis of the vibrational modes at lower wavenumbers, pertaining to the stretching and bending modes of the Fe-C bond in both Fe(II) and Fe(III), as reported in Table 6.

$\nu_{(C\equiv N)}$ in the FeHCF compound features a tail towards lower wavenumbers, which is the consequence of the fast and easy electron exchange of this mixed valence band compound. This tail is also partly visible, although very reduced as for its extension, in the spectra of the other derivatives, a further indication of the occurrence of charge transfer. The easiness of this electronic process is a potential key factor for the applications of these materials in catalysis.

Among the PBAs, CoHCF has been especially studied due to its peculiarities (especially related to its magnetism), while little if nothing has been reported on PBAs featuring a different M. Herein, we have attempted a detailed analysis of the IR spectra of all the materials under investigation, before and after the catalytic tests for CIP degradation, to investigate possible changes induced by the exposure to the catalytic cycle and to the light. While the presence of CIP residual adsorbed on the catalytic materials is not detected, differences in either the position or relative intensities of the $\nu_{(C\equiv N)}$ bands are systematically observed.

In the CoHCF, two main peaks are identified, located at 2090.7 and 2160.1 cm^{-1}, which are ascribed to the stretching vibration of a cyanide ligand bridging Fe(II) and Co(II), and Fe(II) and Co (III), respectively [34]. In the MnHCF, the corresponding vibrations

Table 5
Water content as estimated from thermal analyses.

Sample	Total water content (% weight loss)	Zeolitic water (% weight loss)	Coordinated water (% weight loss)	Coordinated water molecules per formula unit
FeHCF	9.9	0.86	9.0	5.3
MnHCF	22.5	0.57	21.9	7.3
CoHCF	19.2	3.7	15.5	5.5
CuHCF	16.1	2.0	12.7	4.9

Table 6
IR correlation for the hexacyanoferrate/ferrite complexes under investigation, before CIP degradation reaction. Coord: coordinated; HB: hydrogen-bonded; sh: shoulder; s: strong; vs: very strong; w: weak; vw: very weak; br: broad.

Sample		ν(CN) (Fe^{II})	ν(CN) (Fe^{III})	δ(Fe^{II}-C)	ν(Fe^{II}-C)	ν(Fe^{III}-C)	ν$(H_2O)_{coord}$	ν$(H_2O)_{HB}$	δ $(H_2O)_{coord}$	δ$(H_2O)_{HB}$
FeHCF	Before CIP	2061.7 (s, *asym*)	2162.0 (vw)	599.8 (s)	513.0 (sh)	495.7	3624.0 (vw)	–	1600.8 (w)	1645.2 (w)
	After CIP	2050.2 (s, *asym*)	2162.0 (vw)	599.8 (s)	513.0 (sh)	495.7	3624.0 (vw)	–	1600.8 (w)	–
MnHCF	Before CIP	2069.5 (w)	2150.5	653.8 (sh)	530.41	420.5	3641.3	3407.9 (w)	1608.5	1641.3 (vw)
	After CIP	2075.5 (w)	2150.5	632.6 (w)	530.4	420.4	3641.3	3413.9 (br)	1608.5	1649.0
CoHCF	Before CIP	2090.7	2160.1	594.0 (vw)	538.1 (vw)	416.6; 424.3 (sh)	3641.3	3381.0	1608.5	–
	After CIP	2090.7	2162.0	596.0	540.0	430.1 (s)	3643.3	3407.9	1608.5	1677.9
CuHCF	Before CIP	2104.2	2173.6	617.2 (w)	545.8	439.8 (s)	3651.0	3384.8 (br)	1606.6 (w)	1683.7 (vw)
	After CIP	2100.3	2173.6	617.2 (w)	543.9 (s)	441.7 (s)	3649.0 (vw)	3384.8 (w, br)	1606.6	1683.7

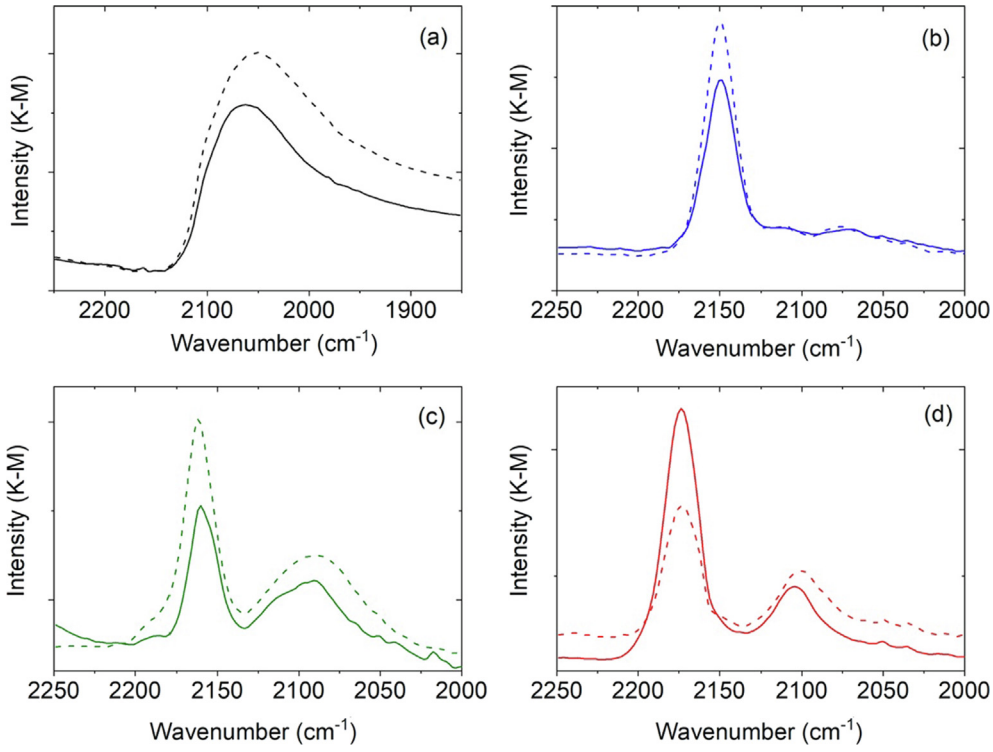

Fig. 6. Detail of the $\nu_{(C\equiv N)}$ stretching region. (a) FeHCF, (b) MnHCF, (c) CoHCF, (d) CuHCF. Solid lines: as-prepared samples; dashed lines: samples after the catalytic test.

Table 7
Fe(II)/Fe(III) ratio before and after CIP degradation reaction, as determined by the analysis of $\nu_{(CN)}$ vibrations retrieved from FTIR spectra.

Sample	Fe^{II}/Fe^{III} Before CIP degradation	Fe^{II}/Fe^{III} After CIP degradation
FeHCF	34.2	173.3
MnHCF	0.0376	0.0351
CoHCF	0.881	0.935
CuHCF	1.18	0.552

are observed at 2069.5 and 2150.5 cm^{-1}, respectively, and are attributed to the stretching of the Fe^{II}-CN-Mn^{II} (high-spin) and Fe^{III}-CN-Mn^{II} (high-spin) [36]. Finally, the CuHCF features these vibrations at 2104.2 and 2173.6 cm^{-1}, which are respectively attributed to Fe^{II}-CN-Cu^{II} and Fe^{III}-CN-Cu^{II}. However, a careful observation of the spectra of the MnHCF evidences the presence of a small band located in between the two major contributions associated with the presence of the second transition metal in its oxidation state + III. Specifically, we detect a signal located at 2110.0 cm^{-1}, which can be ascribed to the presence of Mn in an oxidation state higher than II. Other small vibrations of the cyanide group are visible in the compounds at lower wavenumbers, as previously reported [36].

3.6. Mössbauer analysis

Mössbauer spectroscopy provides useful information on the local interactions between the iron nuclei and their chemical environments. Excluding FeHCF, whose spectrum shows the typical features of PB [37], the bimetallic PBAs show spectra characterized by a broad, slightly asymmetric, intense doublet. Therefore, two different models were used to fit the spectra. FeHCF (Fig. 7 a) was fitted by a four components model; a slightly split doublet, centered at negative velocity values, together with three superimposed doublets, centered at ≈0.38 mm/s. The former doublets show hyperfine parameters (δ: −0.17 mm/s, Δ: 0.12 mm/s, see Table S3 in the Supporting Information for details) ascribable to low spin (LS) Fe(II) according to the literature [37]. The other three doublets are clearly representative of a high spin (HS, S = 1/2) Fe (III) in a distorted octahedral environment. The superimposition of different HS components provides, according to Grandjean [38], a satisfactory description of the vacancies around the Fe(III)

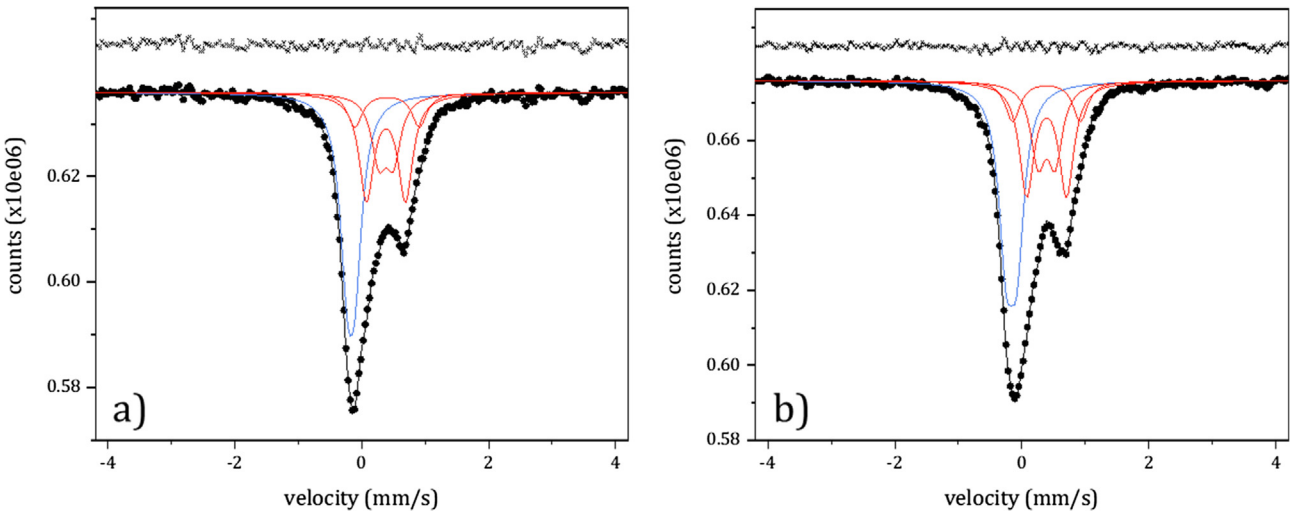

Fig. 7. Mössbauer spectra of FeHCF at RT (a) before and (b) after the reaction with CIP upon light irradiation. Black dots represent the experimental data, the black lines the calculated spectrum, blue lines the LS Fe(II) components, while red lines the HS Fe(III) components. (For interpretation of the references to color in this figure legend, the reader is referred to the web version of this article.)

sites. The spectrum of FeHCF after the reaction with CIP (shown in Fig. 7 b) does not show any substantial difference with respect to that of the as-prepared material. It is well fitted using the same model, and only minor variations of sites population were observed.

Concerning the bimetallic PBAs, several models were tested to fit the spectra and the most consistent one included the presence of a strong doublet together with a weaker and broad doublet (Fig. 8 a, c and e). Both the components show negative δ values as a consequence of the reduction of the 3*d* shielding effect on the *s*-electron by the π-back bonding effect [39]. These evidences, typical for ferro/ferricyanides, suggest the presence of Fe(III) and Fe (II) nuclei in low-spin states (LS, S = 0). The δ values (reported in Table S3 in the Supporting Information) are in agreement with the literature data for PBAs [40–43]. All the ferric doublets show a non-null Δ arising from the distortion in the local octahedral environment of the iron atoms that generate an asymmetry in charge distribution. This evidence can be attributed to the presence of $[Fe(CN)_6]^{4-}$ vacancies and the subsequent coordination of water molecules. Concerning the LS ferrous component, the absence of Δ suggests full occupation of the t_{2g} levels, giving rise to a single line in the Mössbauer spectrum [39]. Also in bimetallic PBAs, the reaction slightly affects the features of their Mössbauer spectra (Fig. 8 b, d and f), allowing the use of the same models to obtain a satisfactory fit. Isomer shift, quadrupole splitting, and linewidth do not show significant variations, and only the site populations seems to be slightly affected.

3.7. Photoinduced charge transfer and spin transition in PBAs

As mentioned, the cyanide ligand is an effective electron shuttle, capable of bridging two transition metal ions featuring an incomplete 3d shell. We showed evidences of the presence of both Fe(II) and Fe(III) in all the complexes under investigation, whose relative amount is changed upon light irradiation, which implies the occurrence of a redox process. On the other hand, we also showed, through infrared spectroscopy, that M^{3+} species are present (with no need of irradiation). This is of particular interest from a catalytic point of view since the possibility of exchanging charges (photogenerated or not), without altering the stability of the material, implies the chance of redox reactions with the surrounding environment. This is true both under dark (as indirectly proved by the catalytic ability shown by the PBAs), and even more, upon light irradiation. The question is then what happens to the electronic configuration of the metals when subjected to light, and subsequently what their spin configuration can become. While the investigation of the details of this aspect is beyond the scope of the present study, it seems relevant mentioning in this context some robust hypothesis to explain the catalytic outcomes.

Electrons stabilization through bonds is a key factor in coordination chemistry and the corresponding spin configuration plays a fundamental role in the chemistry and physics of metal complexes. Previously, when discussing the absorption spectra of the PBAs, we referred to the classic view according to which a homoleptic octahedral complex (of the kind ML_6) features the split of the five d-orbitals into two groups: three orbitals called t_{2g} (non-bonding) and two orbitals called e_g (anti-bonding), as shown in the middle part of Fig. 9 (for a systematic treatment of this topic the reader is referred to fundamental studies in the field, reported for instance in reference [24]). The arrangement of the d-electrons of the metal ion then depends on several factors, including the periodic group and the transitions series, the oxidation state and the strength of the ligand and its cross-talk with the electron pairing energy. This arrangement, which eventually determines the spin state of the complex, is relevant because it as well determines the allocation of electrons in orbitals with different bonding character, thus making them more or less available to be exchanged or even lost. It is also to be mentioned that distortions from this split can occur due to Jahn-Teller effect [44] (represented in the left part of Fig. 9) and, even more relevant in the present case, to the substitution of one of the six L by another ligand, thus resulting in a heteroleptic species (like ML_5Y), which is what we observe in the PBAs due to the presence of coordinated water molecules (and that is confirmed by the appearance of the absorption spectra).

Being cyanide a strong field ligand, according to the classic ligand field theory, we can rather safely assume a low-spin configuration for all the metals involved in PBAs. However, this traditional view (low-spin and high-spin complexes) has been recently questioned by an important essay by Alvarez and Cirera [45]. In their article, the authors state that, in spite of the enormous advances in analytical techniques, the nature of metal complexes (including their stereochemistry, electronic structure and chemical properties) is still poorly understood, and we believe that the

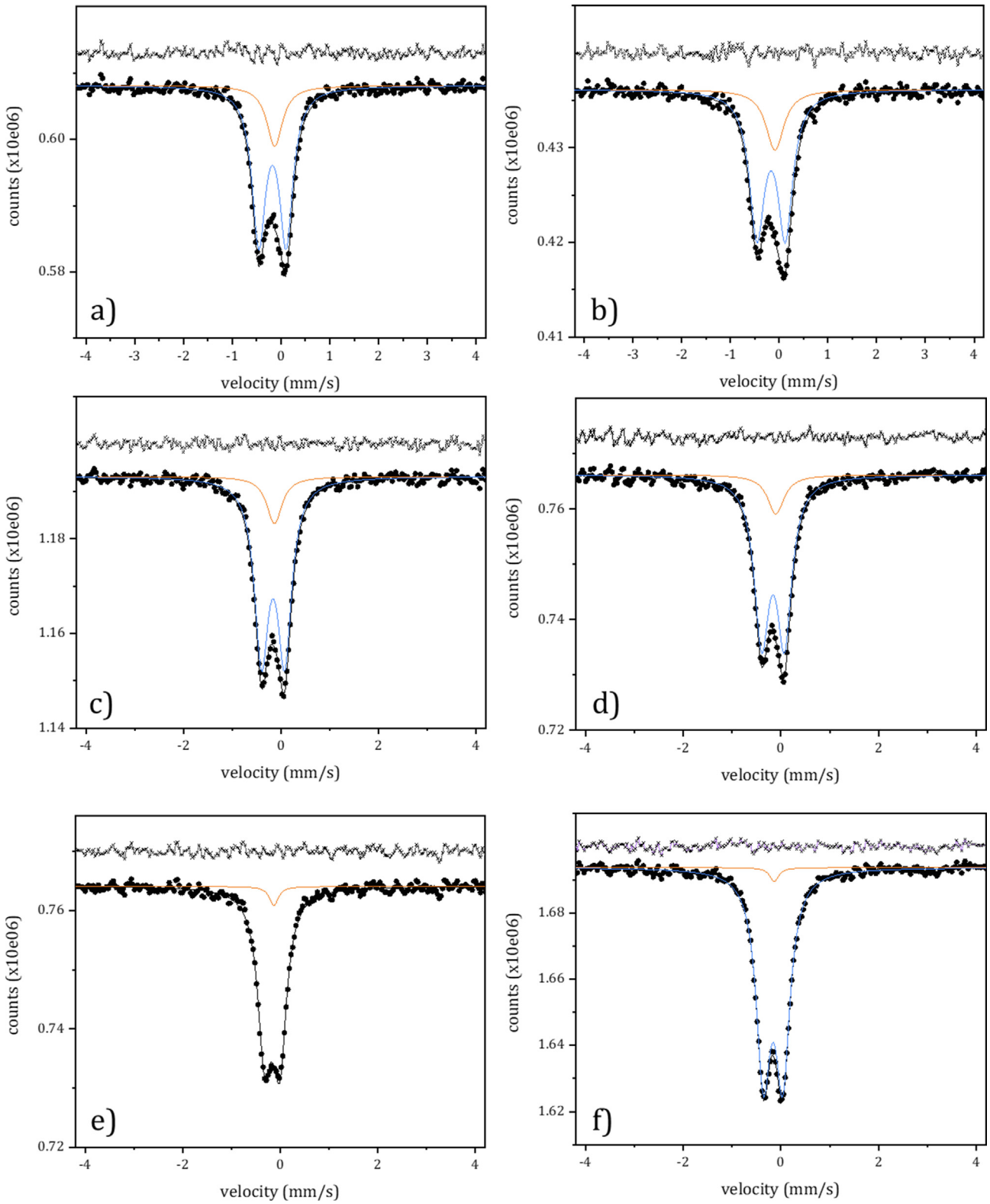

Fig. 8. Mössbauer spectra of CoHCF, CuHCF, and MnHCF at RT before (a, c and e, respectively) and after (b, d and f) the reaction with CIP. Black dots are the experimental data, the black lines the calculated spectrum, blue lines the LS Fe(III) components, while orange lines are the LS Fe(II) components. (For interpretation of the references to color in this figure legend, the reader is referred to the web version of this article.)

experience of the scientific community with the chemistry and photophysics of PB derivatives supports this perception.

Even considering all the PBAs under investigation as low spin complexes, we need to take into account that a change in the metal oxidation state leads to an increase in the electron pairing energy, which can break the low-spin status in favor of a "higher" spin, determining a spin cross-over. On the other hand, a very recent theoretical investigation, confirms the presence of metals in

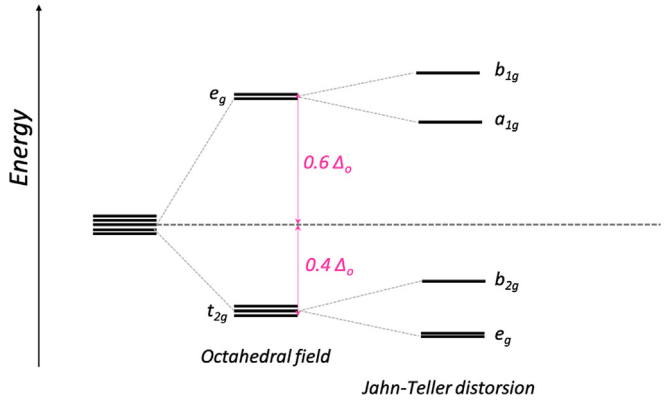

Fig. 9. Relative energies of d-orbitals in an octahedral field, without and with Jahn-Teller tetragonal distortion (elongation).

high-spin configuration [46]. The easiness with which charge exchange can occur in PBAs, coupled with the most classical external stimulus of all, i.e., light excitation, can drastically change the spin status of the materials, supporting the redox processes involved in the catalysis.

Indeed, it is not by chance that we observe a leap forward in the degradation performance of the CoHCF derivative upon light irradiation. Photoinduced charge transfer has been proved in PBAs [47]. The time scale of the process is in the picoseconds, while the lifetime of the photoinduced charges is in the 1–10 μs (depending on the specific analogue). The transfer is also associated with a spin transition of M, determining the existence of two sites: Fe^{II}-CN-M^{III} (low-spin) and Fe^{III}-CN-M^{II} (high-spin) [35]. In our analyses, we could detect the presence of both sites, together with a post-illumination increase in the lattice parameters, which was as well detected in PBAs after the charge transfer-induced spin transition [35]. The situation is however quite complicated, since the electronic state of Co-Fe PBAs depends on the amount of $[Fe(CN)_6]$ sites, so that it is hard to predict what that is in each specific case. Furthermore, different photoswitching pathways have been very recently demonstrated and explored also in case of a RbMnFe PBA [48], evidencing the occurrence of spin transition accompanied by a lattice distortion. On the other hand, other investigations have underlined over time the general character of this intermetallic charge transfer process in compounds where the metals are cyanide-bridged [49–53].

The mentioned studies strongly support the following hypotheses explaining the differences in catalysis observed in the present work.

i) The catalytic site $M(NC)(OH_2)$ binds the CIP molecules via either the carboxylic or carbonyl group (resulting in a 5- or 6-membered ring, among the most stable configurations), probably via a previous ligand dissociation (H_2O). This process occurs in both dark and light conditions.
ii) In particular, we can hypothesize that FeHCF and CuHCF binds the carboxylic group, while a chelation occurs through both functional groups for MnHCF and CoHCF, which can act through an oxidative addition pathway, possessing all the required characteristics (the coordinative unsaturation is provided by the water molecules, which can be favorably exchanged with a stronger ligand, especially if bidentate, thanks to an entropy-driven effect), both metals can access a higher and rather stable oxidation state from M^n to M^{n+2} and possess a non-bonding electron pair.

The steps leading to the loss of the hydroxyl group and, in general, to the rearrangements of molecule fragments to give the reaction product, then occur, promoted, under dark, by a metal–metal charge exchange supported by the CN bridge, where the Fe (II) can give an electron to M, and under light irradiation by the excitation of d-electrons belonging to M. This excitation makes electrons readily available to be transferred to CIP for breaking bonds, while the catalyst is restored thanks to the internal charge transfer process, as further proved by the recyclability tests conducted on CoHCF (the results are shown in Figure S13 in the Supporting Information). These tests show indeed that after five runs CoHCF is still capable of degrading about 70% of the initial amount of CIP in 3 h, upon solar simulated light.

4. Conclusions

Prussian blue derivatives have a well-deserved fame in the field of functional materials. This investigation clearly shows their potential as catalysts for the breaking down of ciprofloxacin at different concentrations and upon different experimental conditions. Thanks to the capability of the C≡N ligands to shuttle charges between two transition metals, the redox processes needed to catalyze the degradation of molecular targets in solution can efficiently occur and be supported. Our study shows that the main feature supporting the catalysis is the possibility of the second transition metal belonging to the derivatives to access different oxidation states, especially when photoinduced excitation occurs.

Although all the materials were found active as catalysts also under dark, light irradiation significantly supports their activity, even changing the reaction mechanisms.

Further investigations are needed to provide definitive proof of the occurrence of a spin cross-over for all the investigated materials, which are however beyond the scope of the present investigation.

The present study demonstrates that, to design effective and selective catalysts, an in-depth knowledge of the materials physical and chemical characteristics is mandatory, coupled with a detailed analysis of the catalytic outcomes, to try and unveil the processes occurring during the transformation of the molecular targets in solution.

Author contributions

SGK performed the catalytic experiments. DN contributed to the materials characterization (EDX, thermal analyses). DOO synthesized the materials. SS and JPM carried out the HPLC-MS analysis. LN was in charge of the Mössbauer analysis. FR analyzed the XRD patterns. IC analyzed the experimental data and wrote the manuscript. All authors have given approval to the final version of the manuscript.

Declaration of Competing Interest

The authors declare the following financial interests/personal relationships which may be considered as potential competing interests: Sepideh G. Khasevani reports financial support was provided by Kempe Foundation. Dickson O. Ojwang reports financial support was provided by Swedish Energy Agency. Dariush Nikjoo reports financial support was provided by AForsk.

Acknowledgment

Kempe Foundation is acknowledged for funding under the project: "Purification platforms for the treatment of pharmaceutical wastes" (Grant No. SMK-1947). DN is grateful for the financial support provided by Åforsk (ref.nr 18-459). DOO is indebted to the Energimyndigheten project: 45517-1 for funding.

Appendix A. Supplementary material

Supplementary data to this article can be found online at https://doi.org/10.1016/j.jcat.2022.04.029.

References

[1] T.G. Ulusoy Ghobadi, E. Ozbay, F. Karadas, How to build prussian blue based water oxidation catalytic assemblies: common trends and strategies, Chem. - A Eur. J. 27 (11) (2021) 3638–3649, https://doi.org/10.1002/chem.202004091.

[2] A. Paolella, C. Faure, V. Timoshevskii, S. Marras, G. Bertoni, A. Guerfi, A. Vijh, M. Armand, K. Zaghib, A review on hexacyanoferrate-based materials for energy storage and smart windows: challenges and perspectives, J. Mater. Chem. A. 5 (36) (2017) 18919–18932.

[3] Z.Y. Yu, Y. Duan, J.D. Liu, Y. Chen, X.K. Liu, W. Liu, T. Ma, Y. Li, X.S. Zheng, T. Yao, M.R. Gao, J.F. Zhu, B.J. Ye, S.H. Yu, Unconventional CN vacancies suppress iron-leaching in Prussian blue analogue pre-catalyst for boosted oxygen evolution catalysis, Nat. Commun. 10 (2019) 1–9, https://doi.org/10.1038/s41467-019-10698-9.

[4] C. Marquez, F.G. Cirujano, C. Van Goethem, I. Vankelecom, D. De Vos, T. De Baerdemaeker, Tunable Prussian blue analogues for the selective synthesis of propargylamines through A3 coupling, Catal. Sci. Technol. 8 (8) (2018) 2061–2065.

[5] Y. Liang, C. Yi, S. Tricard, J. Fang, J. Zhao, W. Shen, Prussian blue analogues as heterogeneous catalysts for epoxidation of styrene, RSC Adv. 5 (23) (2015) 17993–17999.

[6] X. Li, J. Liu, A.I. Rykov, H. Han, C. Jin, X. Liu, J. Wang, Excellent photo-Fenton catalysts of Fe-Co Prussian blue analogues and their reaction mechanism study, Appl. Catal. B Environ. 179 (2015) 196–205, https://doi.org/10.1016/j.apcatb.2015.05.033.

[7] S. Guo, H. Wang, S. Tricard, P. Zheng, A. Sun, J. Fang, J. Zhao, Synthesis of trimetallic Prussian blue analogues and catalytic application for the epoxidation of styrene, Ind. Eng. Chem. Res. 59 (30) (2020) 13831–13840, https://doi.org/10.1021/acs.iecr.0c01715.

[8] H. Lin, Q. Fang, W. Wang, G. Li, J. Guan, Y.i. Shen, J. Ye, F.u. Liu, Prussian blue/PVDF catalytic membrane with exceptional and stable Fenton oxidation performance for organic pollutants removal, Appl. Catal. B Environ. 273 (2020) 119047, https://doi.org/10.1016/j.apcatb.2020.119047.

[9] R. Dossie, The Handmaid to the arts, Printed J. Nourse (1758.).

[10] M. Le Pileur D'Aplogny, Traité des couleurs matérielles et de la manière de colorer relativement aux différents arts et métiers., Saugrain et Laimy, 1779.

[11] A. Salma, S. Thoröe-Boveleth, T.C. Schmidt, J. Tuerk, Dependence of transformation product formation on pH during photolytic and photocatalytic degradation of ciprofloxacin, J. Hazard. Mater. 313 (2016) 49–59, https://doi.org/10.1016/j.jhazmat.2016.03.010.

[12] T.G. Vasconcelos, D.M. Henriques, A. König, A.F. Martins, K. Kümmerer, Chemosphere Photo-degradation of the antimicrobial ciprofloxacin at high pH : Identification and biodegradability assessment of the primary by-products, Chemosphere 76 (2009) 487–493, https://doi.org/10.1016/j.chemosphere.2009.03.022.

[13] A.V. Karim, A. Shriwastav, Degradation of cipro fl oxacin using photo, sono, and sonophotocatalytic oxidation with visible light and low-frequency ultrasound : degradation kinetics and pathways, Chem. Eng. J. 392 (2020), https://doi.org/10.1016/j.cej.2020.124853 124853.

[14] J.A.d.L. Perini, B.F. Silva, R.F.P. Nogueira, Zero-valent iron mediated degradation of ciprofloxacin – Assessment of adsorption, operational parameters and degradation products, Chemosphere 117 (2014) 345–352.

[15] T. An, H. Yang, G. Li, W. Song, W.J. Cooper, X. Nie, Kinetics and mechanism of advanced oxidation processes (AOPs) in degradation of ciprofloxacin in water, Appl. Catal. B Environ. 94 (3-4) (2010) 288–294, https://doi.org/10.1016/j.apcatb.2009.12.002.

[16] X. Yu, J. Zhang, J. Zhang, J. Niu, J. Zhao, Y. Wei, B. Yao, Photocatalytic degradation of ciprofloxacin using Zn-doped Cu2O particles: Analysis of degradation pathways and intermediates, Chem. Eng. J. 374 (2019) 316–327, https://doi.org/10.1016/j.cej.2019.05.177.

[17] J. Zhao, Z. Zhao, N. Li, J. Nan, R. Yu, J. Du, Visible-light-driven photocatalytic degradation of ciprofloxacin by a ternary Mn2O3/Mn3O4/MnO2 valence state heterojunction, Chem. Eng. J. 353 (2018) 805–813, https://doi.org/10.1016/j.cej.2018.07.163.

[18] L. Zhang, J. Tu, L. Lyu, C. Hu, Enhanced catalytic degradation of ciprofloxacin over Ce-doped OMS-2 microspheres, Appl. Catal. B Environ. 181 (2016) 561–569, https://doi.org/10.1016/j.apcatb.2015.08.029.

[19] X.i. Hu, X. Hu, Q. Peng, L.u. Zhou, X. Tan, L. Jiang, C. Tang, H. Wang, S. Liu, Y. Wang, Z. Ning, Mechanisms underlying the photocatalytic degradation pathway of ciprofloxacin with heterogeneous TiO2, Chem. Eng. J. 380 (2020) 122366, https://doi.org/10.1016/j.cej.2019.122366.

[20] N.A. Khan, T. Najam, S.S.A. Shah, E. Hussain, H. Ali, S. Hussain, A. Shaheen, K. Ahmad, M. Ashfaq, Development of Mn-PBA on GO sheets for adsorptive removal of ciprofloxacin from water: Kinetics, isothermal, thermodynamic and mechanistic studies, Mater. Chem. Phys. 245 (2020) 122737, https://doi.org/10.1016/j.matchemphys.2020.122737.

[21] H. Maaoui, P. Kumar, A. Kumar, G.-H. Pan, R. Chtourou, S. Szunerits, R. Boukherroub, S.L. Jain, A Prussian blue/carbon dot nanocomposite as an efficient visible light active photocatalyst for C-H activation of amines, Photochem. Photobiol. Sci. 15 (10) (2016) 1282–1288.

[22] L. K., D.G. Rancourt, Mössbauer spectral analysis software for Windows, version 1., University of Ottawa, 1998.

[23] K.A. Connors, CHEMICAL KINETICS The study of reaction rates in solution, Wiley, 1990.

[24] F.A. Cotton, G. Wilkinson, C.A. Murillo, M. Bochmann, Advanced Inorganic Chemistry, sixth ed., Wiley, 1999.

[25] D.S. McClure, Electronic Spectra of Molecules and Ions in Crystals Part I. Molecular Crystals**Part II will appear in Volume 9 of this series., in: F. Seitz, D. B.T.-S.S.P. Turnbull (Eds.), Academic Press, 1959: pp. 1–47. https://doi.org/10.1016/S0081-1947(08)60478-6.

[26] G. Kortüm, No Title, Z. Physk. Chem. B33 (1936) 243.

[27] D.O. Ojwang, J. Grins, D. Wardecki, M. Valvo, V. Renman, L. Häggström, T. Ericsson, T. Gustafsson, A. Mahmoud, R.P. Hermann, G. Svensson, Structure Characterization and Properties of K-Containing Copper Hexacyanoferrate, Inorg. Chem. 55 (2016) 5924–5934. https://doi.org/10.1021/acs.inorgchem.6b00227.

[28] M. Verdaguer, G.S. Girolami, Prussian Blue analogues, in: Magnetism: Molecules to Materials, Wiley, New York, 2004. https://doi.org/10.1002/9783527620548.ch9d.

[29] S. Ganguli, M. Bhattacharya, Studies of different hydrated forms of Prussian Blue, J. Chem. Soc., Faraday Trans. 1 79 (7) (1983) 1513, https://doi.org/10.1039/f19837901513.

[30] I.E. Åkerblom, D.O. Ojwang, J. Grins, G. Svensson, A thermogravimetric study of thermal dehydration of copper hexacyanoferrate by means of model-free kinetic analysis, J. Therm. Anal. Calorim. 129 (2) (2017) 721–731, https://doi.org/10.1007/s10973-017-6280-x.

[31] D. De Marco, A. Marchese, P. Migliardo, A. Bellomo, Thermal analysis of some cyano compounds, J. Therm. Anal. 32 (3) (1987) 927–937, https://doi.org/10.1007/BF01913779.

[32] S.F.A. Kettle, E. Diana, E.M.C. Marchese, E. Boccaleri, P.L. Stanghellini, The vibrational spectra of the cyanide ligand revisited: The ν(CN) infrared and Raman spectroscopy of Prussian blue and its analogues, J. Raman Spectrosc. 42 (11) (2011) 2006–2014, https://doi.org/10.1002/jrs.2944.

[33] J. Lejeune, J.-B. Brubach, P. Roy, A. Bleuzen, Application of the infrared spectroscopy to the structural study of Prussian blue analogues, Comptes Rendus Chim. 17 (6) (2014) 534–540, https://doi.org/10.1016/j.crci.2014.01.017.

[34] R.O. Lezna, R. Romagnoli, N.R. De Tacconi, K. Rajeshwar, Cobalt hexacyanoferrate: compound stoichiometry, infrared spectroelectrochemistry, and photoinduced electron transfer, J. Phys. Chem. B 106 (2002) 3612–3621, https://doi.org/10.1021/jp013991r.

[35] N. Shimamoto, S.-I. Ohkoshi, O. Sato, K. Hashimoto, Control of charge-transfer-induced spin transition temperature on cobalt-iron Prussian blue analogues, Inorg. Chem. 41 (4) (2002) 678–684, https://doi.org/10.1021/ic010915u.

[36] S. Goberna-Ferrón, W.Y. Hernández, B. Rodríguez-García, J.R. Galán-Mascarós, Light-driven water oxidation with metal hexacyanometallate heterogeneous catalysts, ACS Catal. 4 (6) (2014) 1637–1641, https://doi.org/10.1021/cs500298e.

[37] E. Reguera, J. Fernández-Bertrán, A. Dago, C. Díaz, Mössbauer spectroscopic study of prussian blue from different provenances, Hyperinfe Interact. 73 (3-4) (1992) 295–308, https://doi.org/10.1007/BF02418604.

[38] F. Grandjean, L. Samain, G.J. Long, Characterization and utilization of Prussian blue and its pigments, Dalt. Trans. 45 (45) (2016) 18018–18044.

[39] R. Martínez-García, E. Reguera, J. Rodriguez, J. Balmaseda, J. Roque, Crystal structures of some manganese(II) and cadmium hexacyanoferrates (II, III) and structural transformations related to the sorption of Cesium, Power Diffr. 19 (3) (2004) 255–264, https://doi.org/10.1154/1.1782651.

[40] S. Kjeldgaard, I. Dugulan, A. Mamakhel, M. Wagemaker, B.B. Iversen, A. Bentien, Strategies for synthesis of Prussian blue analogues, R. Soc. open sci. 8 (1) (2021) 201779, https://doi.org/10.1098/rsos.201779.

[41] M. Okubo, D. Asakura, Y. Mizuno, T. Kudo, H. Zhou, A. Okazawa, N. Kojima, K. Ikedo, T. Mizokawa, I. Honma, Ion-Induced Transformation of Magnetism in a Bimetallic CuFe Prussian Blue Analogue, Angew. Chem. 123 (28) (2011) 6393–6397.

[42] H. Yun, T. Guodong, L. Fupei, H. Yanjun, Mössbauer investigation of the thermal phase transition in RbMnFe (CN) 6, 438 (2007) 52–55. https://doi.org/10.1016/j.jallcom.2006.08.039.

[43] E. Reguera, J. Fernandez-Bertran, Effect of the water of crystallization on the Mössbauer spectraofhexacyanoferrate (II and III), Hyperfine Interact. 88 (1994) 49–58, https://doi.org/10.1007/BF02068701.

[44] H.A. Jahn, E. Teller, Stability of Polyatom ic M olecules in D egenerate E lectronic States I-O rbital D egeneracy, Proc. R. Soc. London. 161 (1937) 220–235, https://doi.org/10.1098/rspa.1937.0142.

[45] S. Alvarez, J. Cirera, How high the spin? Allowed and forbidden spin states in transition-metal chemistry, Angew. Chemie – Int. Ed. 45 (19) (2006) 3012–3020, https://doi.org/10.1002/anie.200503492.

[46] K. Hurlbutt, F. Giustino, M. Pasta, G. Volonakis, Electronic structure and electron-transport properties of three metal hexacyanoferrates, (2021). https://doi.org/10.1021/acs.chemmater.1c02183.

[47] S. Zerdane, M. Cammarata, L. Balducci, R. Bertoni, L. Catala, S. Mazerat, T. Mallah, M.N. Pedersen, M. Wulff, K. Nakagawa, H. Tokoro, S.-I. Ohkoshi, E. Collet, Probing Transient Photoinduced Charge Transfer in Prussian Blue Analogues with Time-Resolved XANES and Optical Spectroscopy, Eur. J. Inorg. Chem. 2018 (3-4) (2018) 272–277, https://doi.org/10.1002/ejic.201700657.

[48] G. Azzolina, T. Hiroko, I. Kenta, M. Yoshikiyo, S. Ohkoshi, E. Collet, Chemie, Angew. Chemie – Int. Ed. (2021), https://doi.org/10.1002/anie.202106959.
[49] D.C. Arnett, P. Vihringer, N.F. Scherer, Coherence in an intervalence charge-transfer reaction structure of Prussian blue, J. Am. Chem. Soc. 117 (1995) 12262–12272. http://pubs.acs.org/doi/pdf/10.1021/ja00154a028.
[50] A.V. Tivanski, C. Wang, G.C. Walker, Vibrational mode coupling to ultrafast electron transfer in [(CN) 5OsCNRu(NH3)5]- studied by femtosecond infrared spectroscopy, J. Phys. Chem. A 107 (43) (2003) 9051–9058, https://doi.org/10.1021/jp034274v.
[51] S.-I. Ohkoshi, H. Tokoro, M. Utsunomiya, M. Mizuno, M. Abe, K. Hashimoto, Observation of spin transition in an octahedrally coordinated manganese(II) compound, J. Phys. Chem. B 106 (10) (2002) 2423–2425, https://doi.org/10.1021/jp0133687.
[52] K. Kato, Y. Moritomo, M. Takata, M. Sakata, M. Umekawa, N. Hamada, S. Ohkoshi, H. Tokoro, K. Hashimoto, Direct observation of charge transfer in double-perovskite-like [formula presented], Phys. Rev. Lett. 91 (2003) 3–6, https://doi.org/10.1103/PhysRevLett.91.255502.
[53] S. Chorazy, J. Wang, S.-I. Ohkoshi, Yellow to greenish-blue colour-tunable photoluminescence and 4f-centered slow magnetic relaxation in a cyanido-bridged DyIII(4-hydroxypyridine)-CoIII layered material, Chem. Commun. 52 (71) (2016) 10795–10798.